Available online at www.sciencedirect.com
SCIENCE DIRECT®
International Journal of Heat and Fluid Flow 27 (2006) 730–736
International Journal of HEAT AND FLUID FLOW
www.elsevier.com/locate/ijhff

# Radiated sound and turbulent motions in a blunt trailing edge flow field

Daniel W. Shannon *, Scott C. Morris, Thomas J. Mueller

*Department of Aerospace and Mechanical Engineering, Center for Flow Physics and Control, University of Notre Dame, Notre Dame, IN 46556, USA*

Available online 30 March 2006

**Abstract**

The dipole sound produced by edge scattering of pressure fluctuations at a trailing edge is most often an undesirable effect in turbomachinery and control surface flows. The ability to model the flow mechanisms associated with the production of trailing edge acoustics is important for the quiet design of such devices. The objective of the present research was to experimentally measure flow field and acoustic variables in order to develop an understanding of the mechanisms that generate trailing edge noise. The results of these experiments have provided insight into the causal relationships between the turbulent flow field, unsteady surface pressure, and radiated far field acoustics. Experimental methods used in this paper include particle image velocimetry (PIV), unsteady surface pressures, and far field acoustic pressures. The model investigated had an asymmetric 45° beveled trailing edge. Reynolds numbers based on chord ranged from $1.2\times10^6$ to $1.9\times10^6$. It was found that the small-scale turbulent motions in the vicinity of the trailing edge were modulated by a large scale von Karman wake instability. The broadband sound produced by these motions was also found to be dependant on the "phase" of the wake instability.


*Keywords:* Trailing edge; Acoustics; PIV; Surface pressure; Microphone array

## 1. Introduction

Spatially correlated surface pressures are created by turbulent motions as they convect over a trailing edge. The resultant unsteady surface force causes sound to be radiated to the far field in the form of a dipole source. This phenomena is amplified in the vicinity of a sharp trailing edge. Radiated acoustic energy will depend on the size and convection speed of the turbulent motions as they convect over the trailing edge. The radiated acoustic pressure for low Mach numbers can be expressed in terms of the flow field as a solution to the inhomogeneous wave equation (Howe, 1975, 1998):

$$\nabla^2 B + k_0^2 B = -\nabla\cdot(\vec{\omega}\times\vec{u}), \tag{1}$$

where the source term is the divergence of the vorticity–velocity cross product, $k_0$ is the acoustic wave number, and the variable $B = p/\rho_0 + u^2/2$ consists of the far field acoustic pressure and velocity variables. In the absence of a full solution of the velocity field (e.g., direct numerical simulation), the solution to Eq. (1) can be estimated in a stochastic way by modeling the space–time correlation function of the velocity and vorticity, and relating these functions to radiated sound.

Experimental results are discussed in the following sections in which a unique combination of velocity, vorticity, surface pressure, and acoustic pressure have been measured in the near wake of an asymmetric 45° beveled trailing edge. The chord Reynolds numbers ranged from $1.2\times10^6$ to $1.9\times10^6$ with a corresponding Mach number range of $0.06 < M < 0.09$. The airfoil consisted of a flat strut with a 50.8 mm thickness, a 0.91 m chord, and a 0.61 m span. The leading edge was a 5:1 ellipse and boundary layer trips were placed 1/4 chord length downstream of the leading

* Corresponding author. Tel.: +1 574 631 8408; fax: +1 574 631 8355.
*E-mail addresses:* dshannon@nd.edu (D.W. Shannon), morris.65@nd.edu (S.C. Morris), mueller.1@nd.edu (T.J. Mueller).

0142-727X/$ - see front matter © 2006 Elsevier Inc. All rights reserved.
doi:10.1016/j.ijheatfluidflow.2006.02.017

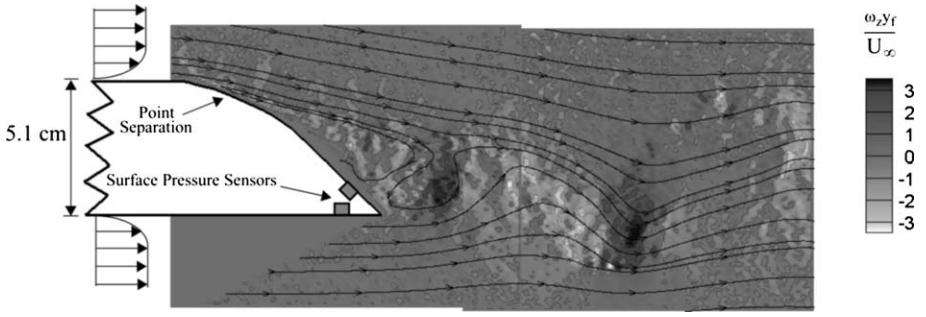


Fig. 1. Instantaneous vorticity field with streamlines. Flow is from left to right. The model has a thickness to chord ratio of 1/18 and an asymmetric 45° beveled trailing edge. Surface pressure sensors are located 12.5 mm upstream of the sharp edge.

edge on both surfaces of the airfoil. The trailing edge geometry is illustrated to the left of Fig. 1. The separation point of the upper boundary layer from the beveled surface is noted, as are the locations of two unsteady surface pressure sensors. This particular trailing edge shape was chosen because it has been used in previous theoretical and experimental works, which are summarized in Blake (1986), Gershfeld et al. (1988) and Blake and Gershfeld (1989). Aeroacoustic simulations have also been computed for this geometry by Wang and Moin (2000).

This project incorporated two experiments. The first experiment used a closed test section wind tunnel and a particle image velocimetry (PIV) system to obtain flow field measurements. These data provided a spatially resolved description of the turbulent velocity and vorticity fields in the near wake. The second experiment was preformed in an anechoic wind tunnel (AWT), an open test section wind tunnel surrounded by an anechoic room. Two free shear layers were located on either side of the test section to allow for the propagation of acoustic waves to the far field. Details about the AWT facility can be found in Mueller et al. (1992). Experiments performed in this tunnel included measurement of the unsteady surface pressure simultaneously with the acoustic pressure. Two unsteady surface pressure sensors were located 12.5 mm upstream of the sharp trailing edge on the suction (upper) surface and pressure (lower) surface of the model. The sound radiated from the test section was measured by a pair of phased microphone arrays.

Sound generated by the trailing edge can be considered to be a superposition of two types of acoustic sources: tonal and broadband. Fig. 2 shows the measured sound pressure level (SPL) spectra measured at a distance of 1.08 m from the center span of the sharp trailing edge in the AWT. The unsteady semi-periodic wake instability associated with the shedding of boundary layer vorticity into the wake is responsible for the narrowband tonal noise generated by the trailing edge. The magnitude of the tonal noise is typically orders of magnitude greater than the broadband noise. A Strouhal number for trailing edge flows was defined by Blake (1986)

$$St \equiv \frac{f \cdot y_f}{U_\infty}, \tag{2}$$

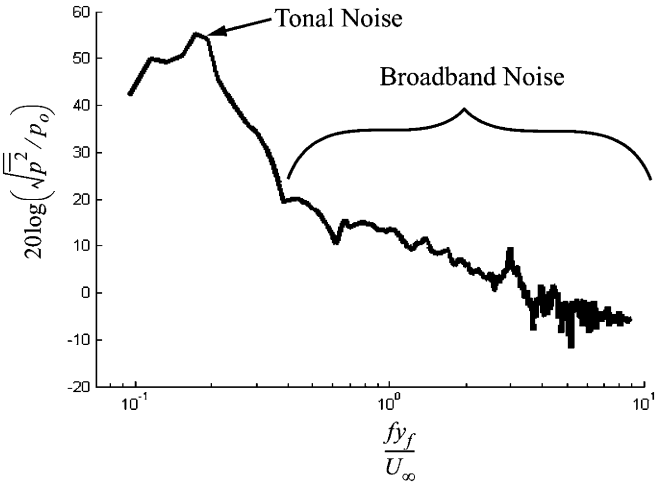


Fig. 2. Sound pressure level spectra as measured by phased arrays. Decibel level referenced to $p_0 = 20$ μPa.

where $f$ is the frequency, $U_\infty$ is the free stream velocity, and $y_f \approx 25$ mm is a wake thickness parameter determined by the minimum distance between the upper and lower shear layers of the wake formed by the separation of the boundary layers. The length scale $y_f$ was utilized because the shedding frequency is only dependent on the size of the separated region. Blake suggests that all trailing edge flows will have a Strouhal number of approximately 0.16. The Strouhal number for the model geometry utilized in this study was found to be 0.184. Smaller scale turbulent motions in the vicinity of the trailing edge cause acoustic scattering at frequencies proportional to their relative size and convection velocities. This phenomenon is responsible for the broadband noise generated by the trailing edge over a wide frequency range. The broadband noise can be observed in Fig. 2 at frequencies higher than the tonal noise.

The following sections will further outline the measurement techniques described above and discuss the results obtained from these measurements.

## 2. Particle image velocimetry

Two component PIV data were obtained in the plane perpendicular to the spanwise direction. Two side-by-side

imaging areas were used in this experiment to provide appropriate spatial resolution while capturing the entire near wake region. Seeding of the measurement area was produced by an aerosol generator that created particles of olive oil ranging in diameter from 0.2 to 1.0 μm. A particle mixer located upstream of the tunnel inlet provided a homogeneous mixture of seeding particles. A LaVision PIV system was used for the data acquisition of this experiment. A pair of 120 mJ Nd:YAG pulse lasers, which generate coherent light at a wavelength of 523 nm, were used to illuminate particles in the test section. A cylindrical lens was used to produce a nominally 1 mm thick light sheet. The laser head was positioned above the test section such that the laser sheet illuminated particles at the mid-span of the airfoil. Images of the particles were acquired using two CCD cameras with $1370 \times 1040$ pixel resolution. Two instantaneous exposures of the measurement area were acquired by each camera with 25 μs in between exposures. The timing of the laser pulses and the camera exposures was controlled by a computer containing a programmable timing unit. The capture rate of the camera system produced approximately three PIV realizations per second.

The velocity vectors were computed using DaVis software by LaVision. An iterative correlation technique was used to compute velocity vectors from the particle movement observed between camera exposures. This technique utilized a shrinking interrogation window algorithm with a final window size of $16 \times 16$ pixels and a 50% window overlap. A vector resolution of 0.83 mm was achieved over an area of approximately $270 \times 107$ mm.

Uncertainty in PIV measurements can be difficult to quantify because it is dependant on the presence of seeding particles, the camera focus, and particle illumination in each interrogation window. As such, the uncertainty can vary over the measurement region and between PIV realizations. An estimate of the uncertainty can be made assuming a subpixel accuracy of 0.1 pixels. This translates to 0.0104 mm particle displacement accuracy, implying that the velocity measurements have an accuracy of approximately 1.4% when compared to the free stream velocity. This estimate agrees well with the root mean square of the measured velocity where the flow was nominally steady.

The vector maps obtained from each PIV realization contained regions of missing data where the absence of seeding particles in an interrogation window made computing the flow velocity impossible. This was more common in regions of the flow where velocity fluctuations and gradients were relatively high. These occurrences, often referred to as gappy data, were limited to an average of 2.4% of the vectors in each realization. Instances of gappy data were eliminated from the data set and ignored when computing velocity statistics.

### 2.1. Instantaneous PIV realization

A single realization of the spanwise component of vorticity with superimposed streamlines is shown in Fig. 1. The trailing edge shape is outlined on the left of the figure. A shadow region, where data are unavailable, is located just below the trailing edge. The magnitude of vorticity has been normalized using the free stream velocity and the wake thickness parameter $y_f$.

The separated flow over the 45° surface contains a region of recirculation. The boundary layer vorticity separating from the model surface creates a von Karman vortex street common to wake flows. The unsteady lift that results from this wake instability is responsible for the tonal noise generated by the trailing edge.

The asymmetry of the trailing edge shape leads to a distinct asymmetry in the convected vorticity field. The positive vorticity that originated from the lower boundary layer, is observed to form compact regions of high circulation near the trailing edge tip, which convect downstream. In contrast, negative vorticity from the upper boundary layer does not exhibit this behavior. Rather, the regions of negative vorticity appear to be distributed between the regions of positive vorticity and are composed of groupings of smaller scale vortical motions.

These observations noted from Fig. 1 and similar observations made from other realizations have led to a number of hypotheses about the nature of the sound produced by this trailing edge. Specifically, the character of the small-scale turbulent motions in the vicinity of the edge appears to be dependent on the "phase" location of the large scale instability. This suggests that the broadband sound produced by the smaller scale motions may also be modulated at the vortex shedding frequency. In the following section, the PIV results will be phase averaged to the vortex shedding phase in order to highlight the features of the turbulent flow that are responsible for tonal versus broadband sound.

### 2.2. Phase averaged PIV

The velocity field can be separated into a phase mean and a fluctuation about that value. This assumes that a period $T$ exists for the vortex shedding process and that each PIV realization is representative of a particular phase in this process. A phase averaged decomposition can be formally written in terms of the vortex shedding phase $\phi$ as

$$u_i(t) = \overline{U_i(\phi)} + u_i'(\phi, t). \tag{3}$$

This is similar to a Reynolds decomposition except that the mean is a function of the vortex shedding phase, and the fluctuations are taken about that mean rather than a time average. The implication of (3) is that the phase mean represents the turbulent motions associated with the vortex shedding instability with all other turbulent scales averaged out. The remaining small-scale turbulent motions are included in the phase fluctuating component of velocity $u_i'(\phi, t)$. Thus, this decomposition allows for the separation the turbulent motions responsible for noise generated in the tonal and broadband frequency regimes. This interpretation is justified given the linearity of the inhomogeneous wave equation (1).

The application of (3) necessitates the determination of $\phi$ for each PIV image. This was accomplished by developing a method using a Karhunen–Loeve (KL) decomposition of the velocity field into its respective eigenmodes. The present application of this decomposition is distinct from proper orthogonal decomposition (POD) (Holmes et al., 1996), although the principal is essentially the same. The stream-wise component of velocity can be represented as

$$u(x,y,t) = \sum_{i=1}^{N} a_i(x,t) \cdot \Phi_i(x,y), \tag{4}$$

where $\Phi_i$ are the discrete eigenvectors determined from the cross-correlation matrix evaluated at each stream-wise position and the coefficient $a_i$ represents the amplitude of mode $\Phi_i$ at each instant of time. For this application the number of discernible eigenvectors was limited to the number of measurement points in the normal direction ($N = 130$). It was found from the present measurements that the first eigenvector was related to the large scale vortical structures generated by the wake instability. Fig. 3 shows the profile of this eigenvector as a function of $y$ nondimensionalized by the model thickness. The projection of this eigenmode onto an instantaneous PIV realization obtained at time $t_0$ produced a spatial distribution of the coefficient $a_1(x,t_0)$, whose value was dependant on the stream-wise distribution of the large scale wake instability observed in Fig. 1. The shedding phase of this PIV realization was determined from an analysis of the phase of $a_1(x,t_0)$. Specifically, the local extrema of $a_1(x,t_0)$ were located and the phase determined by the stream-wise position of the local maxima. The $\phi = 0$ condition was chosen at an arbitrary location in the shedding process. This procedure was repeated for each PIV realization. Additional details about the specific algorithms used to phase average the velocity field can be found in Shannon and Morris (2004).

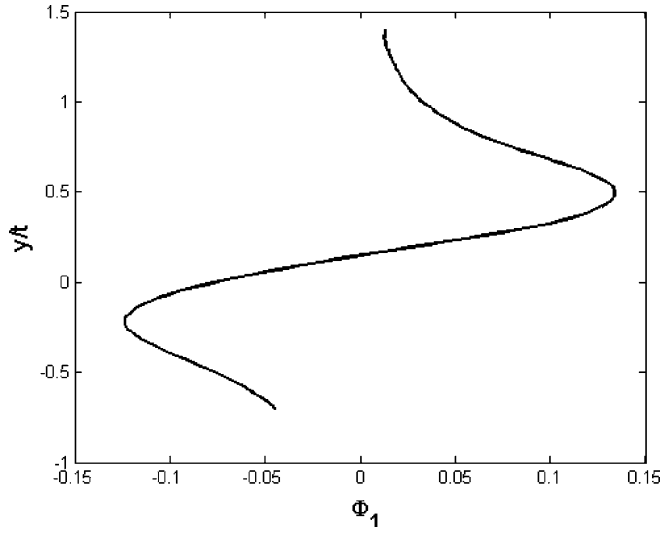


Fig. 3. Profile of the first eigenvector obtained from the Karhunen–Loeve decomposition of the flow field. The $y$ dimension has been nondimensionalized by the model thickness ($t = 50.8$ mm).

Fig. 4 shows an illustration of the phase averaged vorticity field as a function of the vortex shedding phase. As the phase progresses the positive vorticity from the lower boundary layer separates from the model surface, "rolls up" into the low momentum region behind the trailing edge, and convects downstream. These large scale structures remain coherent as they are accelerated downstream. The phase average of the negative vorticity originating from the upper boundary layer forms larger regions of more diffuse vorticity. The compact regions of positive vorticity appear to "impinge" on the negative vorticity as it is shed more gradually into the upper shear layer. This causes the negative (phase averaged) vorticity to be spread relatively uniformly between the compact regions of positive vorticity.

The phase averaged turbulent kinetic energy is defined as

$$k(\phi) = \frac{1}{2}\left(\overline{u_1'(\phi,t)^2} + \overline{u_2'(\phi,t)^2}\right), \tag{5}$$

where the subscripts 1 and 2 represent the phase fluctuating parts of the stream-wise and normal components of the velocity field, respectively. It should be noted that the

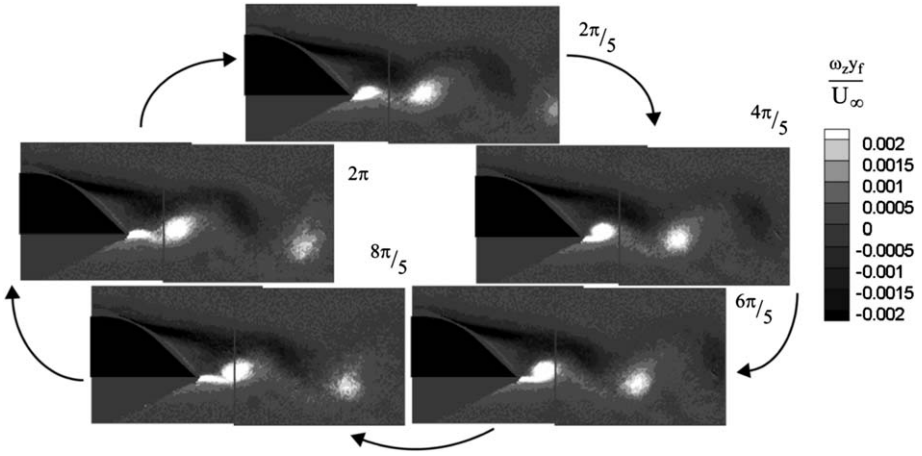


Fig. 4. Contours of vorticity as a function of vortex shedding phase.

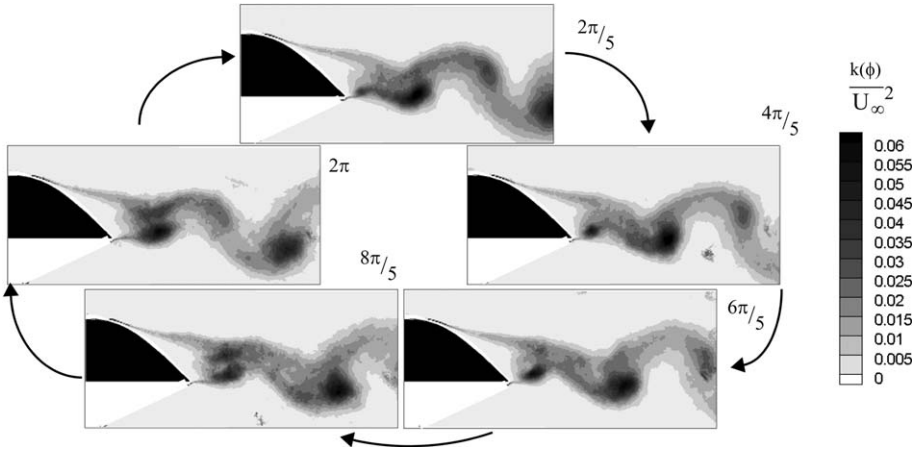


Fig. 5. Contours of turbulent kinetic energy as a function of vortex shedding phase.

contribution of the spanwise component of velocity to the turbulent kinetic energy was ignored because of the absence of velocity data in this direction. The phase averaged $k(\phi)$ values can be interpreted to be the "energy" contained in the turbulent motions that are *not* associated with the vortex shedding. The implication being that $k(\phi)$ is a measure of the relative strength of the motions responsible for the production of broadband noise. Fig. 5 shows the phase averaged turbulent kinetic energy as a function of phase. Although the turbulent motions represented by $k(\phi)$ are distinct from the vortex shedding motions, it is clear from the contours in Fig. 5 that the small-scale fluctuations are a strong function of the shedding phase. Specifically, the magnitude of $k(\phi)$ varies by a factor of 2 or more in the vicinity of the sharp edge. By viewing Figs. 4 and 5 simultaneously it can be observed that the largest values of $k(\phi)$ are associated with the roll up of the lower boundary layer. One could hypothesize that most of the turbulence responsible for broadband acoustic scattering originates from the lower boundary layer as well. This would imply that there may be a stronger correlation between the radiated broadband sound and the small-scale turbulence inherent to the lower boundary layer than would be seen for the upper boundary layer turbulence.

The observations made from the phase averaged vorticity and turbulent kinetic energy further support the notion that the surface pressures and far field acoustics will have a broadband signature that is amplitude modulated at the vortex shedding frequency. These ideas will be further supported in the following section through direct measurements of the surface pressure and the radiated sound field.

## 3. Surface and acoustic pressure measurements

Data acquired in the AWT included simultaneous far field acoustic pressure and unsteady surface pressure. Sound pressure levels were acquired utilizing a phased array consisting of 40 microphones. The array center was positioned 1.08 m from the center span of the sharp trailing edge. General information about phased microphone array design and processing techniques can be found in Underbrink (1995) and Dougherty and Mueller (2002). Information relevant to the specific arrays and measurement techniques used in this project can be found in Olson and Mueller (2004). The unsteady surface pressure was measured utilizing two condenser microphones that were flush mounted to the upper and lower surfaces of the model 12.5 mm upstream of the trailing edge. This location was chosen because most of the acoustic scattering occurs at the sharp edge.

The tonal and broadband frequency contributions to the surface pressure and acoustic pressure signals can be investigated independently. These two "parts" of the time series were separated utilizing a digital Butterworth filter over different frequency ranges. The tonal contributions of a pressure signal $p_{\text{tonal}}(t)$ were identified by band pass filtering the data about the vortex shedding frequency. The result being that only the frequency range related to the large scale wake instability was retained. The broadband contribution of a pressure signal $p_{hp}(t)$ can be investigated by high pass filtering above the vortex shedding frequency. This retained only the frequencies that are related to the smaller scale turbulent motions.

The broadband pressure fluctuations (surface and acoustic) as a function of the vortex shedding phase are of particular interest. The PIV results imply that the small-scale turbulence is modulated by the wake instability. Therefore, the broadband surface pressure and radiated sound pressure, created by this small-scale turbulence, would also be expected to exhibit this dependence on the vortex shedding phase. Phase averaging the high pass filtered pressure signal required a time series of the vortex shedding phase for the data acquired. This was accomplished by computing $p_{\text{tonal}}(t)$ for the signal from the unsteady surface pressure sensor located in the separated region of the trailing edge. The result was a nearly sinusoidal signal whose phase was easily determined. The phase at each instant of time was obtained by finding local extrema of $p_{\text{tonal}}(t)$ and separating the points between local maxima into 15 phase bins. Each measurement point was then assigned to a phase bin such that the broadband pressure

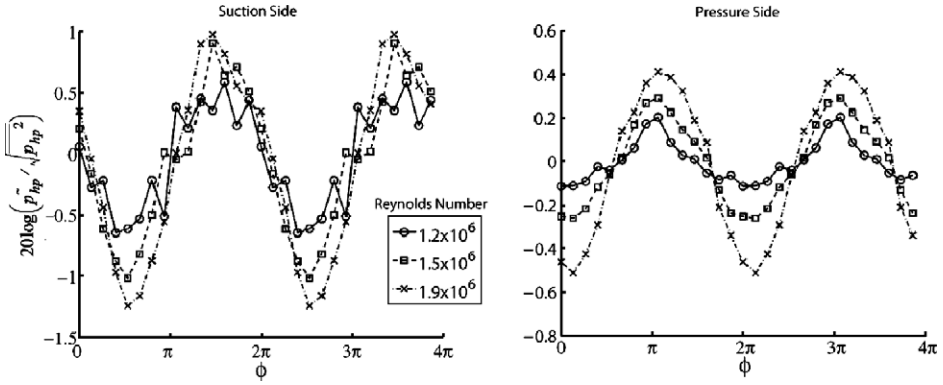


Fig. 6. Phase fluctuating part of broadband unsteady surface pressure signal. Referenced to the broadband root mean square pressure.

fluctuations became a function of both time and phase $p_{hp}(\phi,t)$. The unsteady statistics of $p_{hp}(\phi,t)$ as a function of phase were found by "sorting" the data points into the appropriate phase bins and computing the root mean square value of each bin

$$\tilde{p}_{hp}(\phi) = \sqrt{\overline{p_{hp(\phi,t)^2}}}, \tag{6}$$

where the overbar represents a time average of the realizations for a given $\phi$ value.

### 3.1. Phase averaged surface pressure

Fig. 6 shows the modulation of the root mean square pressure in the broadband frequency range with shedding phase. The data are plotted on a decibel scale referenced to the total root mean square value of the high pass filtered pressure fluctuations $\sqrt{\overline{p_{hp}^2}}$. Two vortex shedding cycles are displayed to show the periodicity of the data. Both surface pressure sensors show an oscillation with the shedding phase. These data demonstrate that the magnitude of the high frequency surface pressure fluctuations is modulated by the vortex shedding process. The modulations observed for the suction side sensor are observed to be larger that those on the pressure side. The higher momentum fluid attached over the pressure side sensor may not be as easily distorted by the vortex shedding motions as the fluid in the stagnant separated region.

The broadband surface pressure modulation appears to be a function of the Reynolds number. This dependence is curious because the phase modulations observed in Fig. 6 have been normalized by the total broadband surface pressure fluctuations. This suggests that for flow regimes where vortex shedding is present the amplitude modulation of broadband sound may be more prevalent at larger Reynolds numbers.

### 3.2. Phase averaged acoustic pressure

The phase modulation of the broadband noise measured by the phased microphone array is illustrated in Fig. 7. It

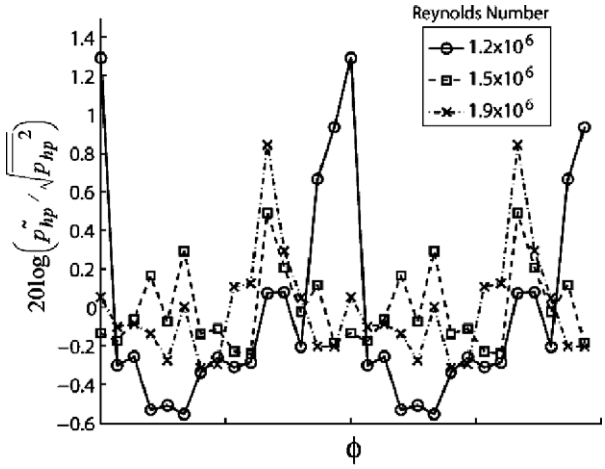


Fig. 7. Broadband sound as a function of vortex shedding phase. Referenced to the broadband root mean square pressure.

can be seen that the oscillations about the phase mean were not as sinusoidal as was observed for the surface pressure. Rather, the oscillations remain below the phase mean for the majority of the shedding cycle and then "spike" well above this threshold for approximately 3/8 of the cycle. An apparent phase shift of the broadband "spike" was also observed for the lowest Reynolds number case. The same Reynolds number dependence of the phase averaged surface pressure seen in Fig. 6 was not observed for the phase averaged broadband noise. This may have resulted from the increase of unwanted (parasitic) sound produced by the operation of the AWT at the higher free stream velocities. However, the hypothesis of modulated broadband noise due to the large scale vortex shedding is still supported by these results.

## 4. Conclusions and discussion

Spatially resolved velocity data collected in the near wake of a trailing edge have revealed the presence of an asymmetric von Karmen wake instability. Phase averaging

these data with respect to the vortex shedding has allowed for the separation the turbulent motions responsible for noise generated in the tonal and broadband frequency ranges. It was observed from the instantaneous and phase averaged velocity data that the character of the small-scale turbulence in the vicinity of the sharp trailing edge was dependant on the phase of the vortex shedding motions. The broadband unsteady surface pressure and far field acoustic pressure generated by these motions would also be expected to be a function of the shedding phase. Modulations of the magnitude of the surface and far field acoustic pressure fluctuations with vortex shedding phase were observed for measurements taken in an anechoic wind tunnel.

The implication of the phase modulation of smaller turbulent scales by the vortex shedding is that the turbulent length scales relevant to the propagation of acoustic pressure waves will also be a function of the phase. This may be an influential factor to account for when modeling the sound generated by a trailing edge flows with vortex shedding. The behavior of the far field acoustics about a phase reference could be an important feature in the modeling of trailing edge noise.

## Acknowledgements

This research was made possible through funding from the US Office of Naval Research under Grant No. N00014-03-1-0105. The technical monitor was Ron Joslin. The technical consultation of William K. Blake is gratefully acknowledged.

## References

Blake, W.K., 1986. Mechanics of Flow-Induced Sound and Vibration, vol. II. Academic Press, New York.

Blake, W.K., Gershfeld, J.L., 1989. The Aeroacoustics of Trailing Edges, Frontiers in Experimental Fluid Mechanics (A90-26059 10-34). Springer-Verlag, Berlin, pp. 457–532.

Dougherty, R., Mueller, T.J. (Eds.), 2002. Beamforming in Acoustic Testing. Aeroacoustics Measurements. Springer-Verlag, Berlin, pp. 62–97.

Gershfeld, J.L., Blake, W.K., Knisely, C.W., 1988. Trailing edge flows and aerodynamic sound. In: AIAA Thermophysics, Plasmadynamics and Lasers Converence, San Antonio, TX, pp. 2133–2140 (88-3826-CP).

Holmes, P., Lumley, J.L., Berkooz, G., 1996. Turbulence, coherent structures, dynamical systems and symmetryCambridge Monographs on Mechanics. Cambridge University Press, Cambridge.

Howe, M.S., 1975. Contributions to the theory of aerodynamic sound, with application to excess jet noise and the theory of the flute. Journal of Fluid Mechanics 71, 625–673.

Howe, M.S., 1998. Acoustics of Fluid–Structure Interactions. Cambridge University Press, Cambridge.

Mueller, T.J., Scharpf, D.F., Batill, S.M., Strebinger, R.B., Sullivan, C.V., Subramania, S., 1992. A new low speed wind tunnel for acoustic measurements. Proceedings of the European Forum on Wind Tunnels and Wind Tunnel Test Techniques. Royal Aeronautical Society.

Olson, S., Mueller, T.J., 2004. Phased array acoustic imaging of an airfoil trailing edge flow. In: 11th International Symposium on Flow Visualization, Notre Dame, IN.

Shannon, D.W., Morris, S.C., 2004. Visualization of blunt trailing edge turbulence. In: 11th International Symposium on Flow Visualization, Notre Dame, IN.

Underbrink, J.R., Practical considerations in focused array design for passive broad-band source mapping applications. Masers Dissertation, Acoustics Department, Pennsylvania State University, Philadelphia, PA, 1995.

Wang, M., Moin, P., 2000. Computation of trailing-edge flow and noise using large-eddy simulation. AIAA Journal 38, 2201–2209.